Nanoscale Advances

ROYAL SOCIETY OF CHEMISTRY

PAPER

Cite this: *Nanoscale Adv.*, 2025, 7, 2368

Effect of molecular adsorption on the conductivity of selectively grown, interconnected 2D-MoS_2 atomically thin flake structures

Ionel Stavarache, *[a] Catalin Palade,[a] Adrian Slav,[a] Ioana Dascalescu,[a] Ana-Maria Lepadatu,[a] Elena Matei,[a] Cristina Besleaga,[a] Magdalena Lidia Ciurea,[ab] Beata E. Kardynal*[cd] and Toma Stoica *[a]

The gas sensitivity of field-effect structures with 2D-MoS_2 channels selectively grown between Mo electrodes using the Mo-CVD method was investigated by measuring the effect of molecular adsorption from air on the device source-drain current (I_{sd}). The channels were composed of interconnected atomically thin MoS_2 grains, with their density and average thickness varied by choosing two different distances (15 and 20 μm) between the Mo contacts. A high response to the tested stimuli, including molecule adsorption, illumination and gate voltage changes, was observed. A significant, persistent photoconduction was induced by positive charge accumulation on traps, most likely at grain boundaries and associated defects. I_{sd} increased under high vacuum, both in the dark and under illumination. The relative dark current response to the transition from air to high vacuum reached up to 1000% at the turn-on voltage. When monitored during the gradual change in air pressure, I_{sd} exhibited a non-monotonic function, sharply peaking at about 10^{-2} mbar, suggesting molecular adsorption on different defect sites and orientations of adsorbed H_2O molecules, which were capable of inducing electron accumulation or depletion. Despite the screening of disorder by extra electrons, the #20 μm sample remained more sensitive to air molecules on its surface. The high vacuum state was also investigated by annealing devices at temperatures up to 340 K in high vacuum, followed by measurements down to 100 K. This revealed thermally stimulated currents and activation energies of trapping electronic states assigned to sulfur vacancies (230 meV) and other shallow levels (85–120 meV), possibly due to natural impurities, grain boundaries or disorder defects. The results demonstrate the high sensitivity of these devices to molecular adsorption, making the technology promising for the easy fabrication of chemical sensors.

Received 10th February 2025
Accepted 21st February 2025

DOI: 10.1039/d5na00138b

rsc.li/nanoscale-advances

1. Introduction

Strong interactions of nanometer-thick layers of transition metal dichalcogenides (2D-TMDs) and other 2D materials with light, along with their good electronic transport properties, have led to a large number of reported potential applications.[1–4] In atomically thin 2D-MoS_2 layers, a strong increase in exciton binding energy, dielectric confinement, spin–orbit coupling and large valence band spin-splitting strongly influence the electronic properties, making it attractive for photonics and spintronics.[5–8] The monolayer (ML) of 2H-MoS_2 consists of an atomic Mo layer cladded by two S layers. In a trigonal arrangement of atoms, the ML of 2H-MoS_2 is a semiconductor with a direct bandgap of about 1.9 eV. The 2D-MoS_2 with multilayers (MLs) remains a semiconductor, but the bandgap becomes indirect and decreases with the number of ML layers, reaching a value of 1.2 eV in the bulk material. Through different arrangements of the atomic layers, other phases are formed: 3R (rhombohedral) semiconducting and 1T (orthogonal) metallic.[9–11] The 2H-MoS_2 phase is the most thermodynamically stable.

The high surface-to-volume ratio and high ON/OFF current ratio in field-effect transistors (FETs) make 2D-MoS_2 FETs suitable for highly sensitive optical bio- and gas sensors.[12–14] Multicolor sensors and improved photovoltaic efficiency in solar cells can be obtained by alloying and forming heterostructures of different 2D-TMDs.[15–17] Due to their chemical and mechanical stability, ultrathin 2D-MOS_2 devices can be fabricated on different substrates, including flexible ones, for applications in electronics and optoelectronics as light emitters

[a]National Institute of Materials Physics, 405A Atomistilor Street, 077125 Magurele, Romania. E-mail: stavarache@infim.ro; toma.stoica@infim.ro
[b]Academy of Romanian Scientists, 54 Splaiul Independentei, 050094 Bucharest, Romania
[c]Peter Grünberg Institute 9, JARA-FIT, Forschungszentrum Jülich, 52425 Jülich, Germany. E-mail: b.kardynal@fz-juelich.de
[d]Department of Physics, RWTH Aachen University, 52074 Aachen, Germany

or detectors.[18–21] They can also be used in various electrochemical applications, such as batteries, supercapacitors, and catalytic electroreduction.[22–26] The modification of 2D materials by heteroatoms or molecules through doping, intercalation or surface modification opens a wide perspective to tune the properties of 2D materials for many applications such as magnetic, electrical, photoelectric, energy storage and conversion.[13,27]

Different strategies for doping of 2D metal chalcogenides have been employed, as follows: (i) substitutional doping, (ii) charge transfer doping, (iii) intercalation doping and (iv) electrostatic field-effect doping.[28] Atoms, molecules, particles, support substrate or cladding layers can interact electrostatically with 2D materials and change their carrier concentration. They can change the charge state of defects, affecting the electronic transport through films. Both effects can be influenced by light.[29] Exfoliated ML flakes of 2D-MoS_2 and 2D-WSe_2 have been reported to show a 50- and 3-fold increase in photoluminescence, respectively, after removing the adsorbed air molecules by annealing at 450 °C under vacuum. The photoluminescence increased by a factor of 100 in 2D-MoS_2 but decreased significantly in 2D-WSe_2 upon exposure to pure H_2O and/or an O_2 atmosphere.[30] Dipole-induced molecular doping has been shown to lead to the accumulation or depletion of electrons depending on the orientation of the molecular dipole in the collective molecular functionalization of monolayer MoS_2.[31] Through simulation, the different adsorption sites preferred by these molecules were identified, for which the adsorption energy is negative, where the more negative, the more stable the adsorption.[32–34] Defect sites and sites at or close to the edges are clearly preferable adsorption sites. The O_2 molecule preference site is on top of Mo, where it receives more electrons. In the case of H_2O, there are more favorable sites and molecule orientation with adsorption energy controlled by O–Mo and H–S attractive interactions, but also O–S and H–Mo repulsive interactions.[31,32] Another possibility exists for H_2O molecules, *i.e.*, chemisorption by dissociating water into H and OH bound at different sites.[33] H_2O and O_2 adsorption usually induces electron depletion in the MoS_2 layer, but in the case of H_2O with multiple adsorption sites and molecule orientations, it can also induce electron accumulation, at least as a temporary unstable adsorption effect. Also, the formation of clusters of H_2O dipolar molecules adsorbed on the surface of 2D-MoS_2 can in principle work as collective dipole doping similar to that described in ref. 31.

The electrostatic and/or chemical interaction of molecules adsorbed on atomically thin 2D-MoS_2 layers constitutes the working principle of highly sensitive FET detectors for inorganic or organic molecules.[13,14,35–39] However, the fabrication of 2D-MoS_2 FET sensors is generally based on isolated 2D flakes obtained either by exfoliation from bulk materials or CVD deposition with random nucleation on the support surface.[40] The fabrication of FET electrodes requires the localization of the flakes and the expensive, slow electron beam lithography technique, and thus cost-effective processes need to be developed to make these devices viable technology beyond lab tests.

The device sensitivity to molecule adsorption is enhanced in FETs with a high density of edge and boundary defects as preferential adsorption sites.[32–34] However, a high density of defects inside and on the surface of MoS_2, as well as at the substrate interface has an important charge trapping effect, which strongly affects the field effect characteristics, inducing large hysteresis through electronic and molecular trapping–detrapping phenomena, resulting in a low-level source-drain dark current and reduced mobility. In addition to the quality of the 2D-MoS_2 material, the performances of FETs depend on their fabrication method and the used measurement conditions (contact resistance, free surface passivation, measurement atmosphere, history of external stimuli, *etc.*). Thus far, it is generally accepted that 2D-MoS_2 with the best crystalline quality is obtained in flakes exfoliated from the bulk material. However, the electron mobility values reported in the literature for measurements on single exfoliated flake 2D-MoS_2 FETs vary over a wide range of 0.1–200 $cm^2\ V^{-1}\ s^{-1}$.[41,42] The balance between intrinsic doping and the density of trapping centers depends on the 2D-MoS_2 fabrication method and its optimization. By introducing structural defects through the optimal incorporation of 1T metallic domains into exfoliated 2H-MoS_2 flakes by a mild oxygen plasma treatment to increase the layer conductivity, a high field-effect mobility of 237 $cm^2\ V^{-1}\ s^{-1}$ was achieved compared to 7–43 $cm^2\ V^{-1}\ s^{-1}$ in the pristine flakes.[43] In contrast, due to the trapping defects induced by exposure to oxygen above 2 mbar pressure, the hysteresis of the transfer characteristics of the exfoliated multilayer FETs strongly increased, while the mobility was significantly reduced from 52 to 15 $cm^2\ V^{-1}\ s^{-1}$.[44] The hysteresis in the transfer characteristics of 2D-MoS_2 low mobility FETs (0.3–6 $cm^2\ V^{-1}\ s^{-1}$) and its correlation with the charge trapping and the exposure to H_2O and O_2 effects, as well as the energy position of the trapping levels in the gap have also been intensively investigated in a series of publications.[45–47] Employing gold-assisted mechanical exfoliation, ultra-large monolayers (on the centimeter scale) were obtained on an Al_2O_3/Si substrate, exhibiting a compressive strain of −0.25%, n-doping of $\approx 5 \times 10^{12}\ cm^{-2}$ and mobility of 2.3 $cm^2\ V^{-1}\ s^{-1}$.[48] Films of interconnected (edge-to-edge contact) MoS_2 exfoliated nanoflakes were produced on a large area by self-assembled tiling at the planar interface between two immiscible liquids, exhibiting an FET mobility of 0.73 $cm^2\ V^{-1}\ s^{-1}$.[49] MoS_2 exfoliated nanosheet FETs were measured with a four-terminal electrical device to eliminate any contact contributions and reported in ref. 50, showing that there are two classes of FET mobility with distinct behavior. Specifically, the mobility decreases (increases) with temperature due to dominant phonon scattering (due to impurity scattering and high contact resistance) in devices with room temperature (RT) mobility higher (lower) than 30 $cm^2\ V^{-1}\ s^{-1}$. To avoid direct contact of MoS_2 with the photoresist and the ambient environment during the FET fabrication process, an SiO_2 protective layer was used, which was selectively etched on the contact areas to improve the FET contacts, thus achieving a mobility of 42 $cm^2\ V^{-1}\ s^{-1}$. This was ∼20 times higher compared to the mobility of the MoS_2 FET fabricated without the SiO_2 protective layer.[51] Intentionally aged 2D-MoS_2 FETs showed a significant

decrease in electron mobility to 0.5 $cm^2\ V^{-1}\ s^{-1}$ compared to that of the as-fabricated devices of up to 8 $cm^2\ V^{-1}\ s^{-1}$, but better device stability working as a selective gas sensor by detecting the current variation and low-frequency noise induced by exposure to air and vapors of polar and non-polar solvents.[52] The trapped charges and related hysteresis giving rise to the unscreened Coulomb scattering and/or the variable range hopping in MoS_2 FETs were also studied in ref. 47. CVD-grown 2D-MoS_2 using sulfur in the gas phase as the precursor showed an average FET mobility value of 0.12 $cm^2\ V^{-1}\ s^{-1}$ for the sulfurization of very thin Mo metal films, while in the case of the Mo oxide film, a very low mobility of 10^{-4} $cm^2\ V^{-1}\ s^{-1}$ was reported.[41,53,54]

The selective growth of 2D-MoS_2 at predefined positions on the surface of supports is one of the promising solutions for the mass production of 2D-MoS_2 FET devices. The nucleation and selective CVD growth of MoS_2/WSe_2 on c-Al_2O_3 or a-HfO_2 was demonstrated using vapor precursors of sulfur and oxides of Mo and W and a sacrificial SiO_2 mask with several-micron-wide windows.[55] The selective growth of 2D-MoS_2 has also been achieved on structured Mo supports *via* CVD deposition with sulfur vapor and Mo oxide as the precursors, where the oxide is either from MoO_3 powder or the oxidation of Mo pads by oxygen from vacuum leaks.[56,57] In principle, selective growth at the desired sites can be also achieved *via* the sulfurization of MoO_x thin films pre-deposited through a photolithographic mask, but this process still requires further optimization to reduce the MO_2 doping at high temperatures and improve the film uniformity, while maintaining a low oxide sublimation rate.[58–61] The selective nucleation and growth of 2D-MoS_2 around oxide windows on structured SiO_2/Si supports was achieved by vapor transport deposition directly from MoS_2 powder.[62] The films consisting of multi-crystalline flakes with the range of sizes and density nucleated and grew around the substrate patterns. Better control of the selective nucleation of 2D-MoS_2 at the proximity of Mo electrodes was obtained by the simultaneous diffusion of Mo native oxide from the Mo electrodes and its reaction with sulfur vapors (Mo-CVD method).[63] An additional advantage of this growth method is its bottom-up approach for fabricating devices, where the source-drain Mo-electrodes are pre-deposited and an MoS_2 film is self-aligned and in intimate contact with them, without post-growth photolithographic process, avoiding the surface contamination with resists after common the photo- or electron-beam device fabrication, which is very important for the fabrication of gas sensors.[64–66] The photo-FET devices prepared using this method showed a responsivity of 25 $A\ W^{-1}$ and more than 4 orders of magnitude variation in the photo-to-dark current ratio, which was adjustable by changing the gate voltage. The field-effect structures fabricated by this simple method can be used for various applications, such as the detection of adsorbed molecules, but to the best of our knowledge, there are no reports of these studies.

In this work, we investigated the response to adsorbed air molecules on selectively grown 2D-MoS_2 interconnected flakes obtained *via* the Mo-CVD method with pre-deposited Mo electrodes. The FETs were fabricated in the simplest way, by directly bonding the contacts after the growth of 2D-MoS_2, avoiding surface contamination with photoresist traces through any additional photolithographic metallization process. The selectively grown 2D-MoS_2 layers covered the gap between the Mo source-drain contacts of the field effect structures, ensuring not only the selective growth in the active areas, but also intimate contacts with the pre-deposited Mo electrodes. We studied the devices with electrodes spaced at 15 μm and 20 μm, which we referred to as #15 μm and #20 μm, respectively, and expected to have different densities and average thickness of MoS_2 flakes given that they were grown using the same growth parameters. The desorption of molecules from the air (O_2 and H_2O) by exposure to high vacuum (HV) resulted in an increase in both the dark and photo-currents compared with that measured at atmospheric pressure. Both the #15 μm and #20 μm samples exhibited similar behavior when measured during vacuum annealing at 340 K and subsequent measurements of the current-temperature dependence at low temperatures down to 100 K. We propose that depending on the orientation of the adsorbed H_2O molecules from the air and the adsorption sites on the 2D-MoS_2 layer, one can observe the accumulation (at least as temporary effect) or depletion of electrons in MoS_2.

2. Experimental methods

2.1 Sample fabrication

To prepare the growth substrate, an Mo layer with a thickness of 30 nm was deposited by magnetron sputtering of SiO_2 (300 nm)/c-Si and patterned by the photolithographic liftoff process to form multi-finger contacts to be used in FETs as source-drain contacts, as illustrated in Fig. 1a by the bottom bird's eye view image. Each contact consisted of a large square pad of 500 μm side and a number of fingers that fit along the lateral length of the pad. The Mo fingers were spaced at 15 μm or 20 μm, defining the channel length L of the FET device. The overlap of the opposing source and drain fingers was designed to be $W_i = 40$ μm, corresponding to an active area of selectively grown 2D-MoS_2 of $L \times W_i$ for each overlapping region of the opposing fingers (see a detailed image of the selective growth in Fig. 1b). The total channel width of the FET is the sum of all the finger overlap regions $W = \sum_i W_i$, which corresponds to a total active area measured in squares of side L (W/L) of 48 and 28 for the #15 μm and #20 μm samples, respectively. The selective growth of atomically thin MoS_2 with Mo supplied from the deposited layer was obtained by the Mo-CVD method in a 3-zone horizontal quartz tube furnace (Carbolite HZS). The growth substrate was placed in the higher temperature (750 °C) zone of the furnace, while the crucible with sulfur powder was placed in the low temperature (200 °C) zone. The selective growth took place over 30 min by simultaneous surface diffusion of native MoO_2 from the Mo surface and its chemical reaction with S vapor transported by 20 sccm Ar flux at 100 mbar pressure. Once the growth was finished, the FET device was completed by making a GaIn ohmic contact on the backside of the Si substrate, which was used as the gate electrode. More details can be found in ref. 63.

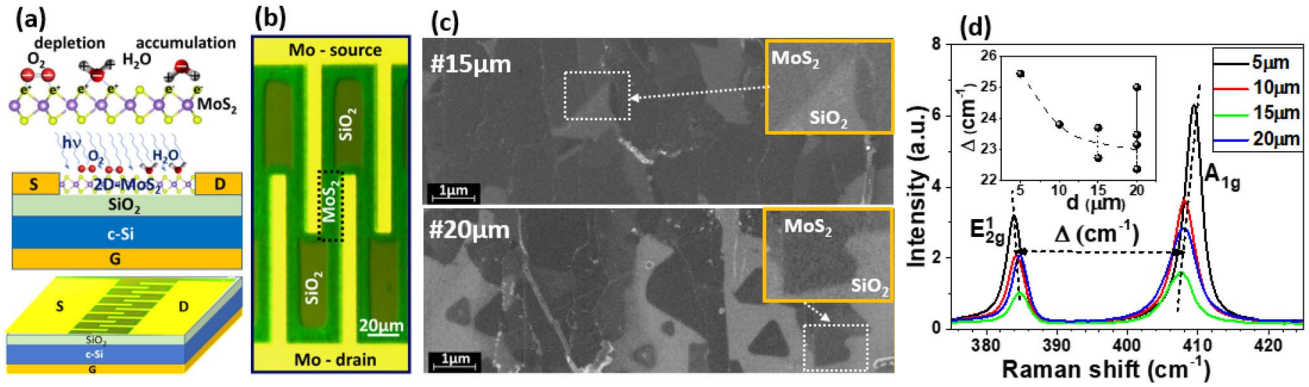

Fig. 1 (a) Schematic of the electron depletion and accumulation in 2D-MoS_2 due to the adsorption of O_2 and H_2O molecules from air, showing the cross-section and bird's-eye view of the device with selectively grown MoS_2 between Mo finger contacts; (b) optical image detail of selectively grown 2D-MoS_2 around Mo finger contact patterns; (c) comparison of high-resolution SEM images of 2D-MoS_2 acquired from the gap between Mo electrodes for #15 μm and #20 μm samples (dark areas – MoS_2 MLs; lighter areas – SiO_2); (d) representative Raman spectra of 2D-MoS_2 for different gap lengths (inset shows the dependence of Δ between A_{1g} and E^1_{2g} peaks as a function of gap length).

2.2 Morphology, structure and photosensitivity characterization methods

The morphology of the selectively grown films was investigated by optical and scanning electron microscopy (SEM) (Zeiss Gemini 500). The information about the nature of the crystalline structure and the layer thicknesses was obtained from Raman spectroscopy, using a LabRAM HR (Horiba Jobin-Yvon) with 532 nm excitation. The source-drain current, I_{sd}, as a function of the source-drain, V_{sd}, and gate, V_g, voltages was monitored under monochromatic light with the wavelength above the absorption edge. Transimpedance characteristics (I_{sd} as a function of V_g for a set V_{sd}) were recorded using a Keithley 236 Source Measure Unit and a Keysight B2902A Source Measure Unit. A Newport Cornerstone™ 260 monochromator was used for sample illumination. All measurements presented herein were performed in a cryostat, in air and/or vacuum, at room temperature without any prior annealing, except for those in the last Subchapter 3.4 regarding the temperature dependence of the current in the range of 100–240 K when the samples were first treated under high vacuum up to 340 K.

3. Results and discussion

A schematic diagram of the used field-effect device with source-drain finger contacts is shown in Fig. 1a. Under ambient pressure, air molecules are adsorbed on the surface of MoS_2, modifying its conductivity *via* the trapping of charges or electrostatic charging of the layers. O_2 and H_2O molecules are the most often considered adsorbates. As shown in the Introduction, the adsorption of H_2O and O_2 usually induces electron depletion in the MoS_2 layer, but in case of H_2O molecules with multiple adsorption sites and orientations, electron accumulation can also be induced (sketch in Fig. 1a).

2D-MoS_2 was selectively grown around Mo patterns *via* the Mo-CVD method described in ref. 63. Employing this method, MoS_2 layers with intimate contact with the Mo patterns were obtained through simultaneous processes of diffusion and sulfurization of the oxide previously formed on the Mo surface. The details of the Mo finger contact patterns are exemplified by the optical image in Fig. 1b (MoS_2 layer (green contrast) surrounds the Mo contacts (yellow)). We succeeded in selectively growing MoS_2 up to a distance of 10–15 μm from the Mo pads, which was sufficient for 2D-MoS_2 to cover the space between the source-drain Mo finger contacts, as marked in Fig. 1b, up to a gap of 20 μm. This structure grown on conductive Si substrate covered by a 300 nm SiO_2 isolation layer can be used as a field effect transistor with Mo source-drain contacts and Si substrate as the back gate.

The selectively grown 2D-MoS_2 layer consisted of interconnected flakes of different thicknesses, ranging from single ML to a stack of few ML.[63] The interconnected MoS_2 flakes formed conductive layers between the Mo source-drain finger contacts dominated by many grain boundaries and flake edge defects. The density of the flakes and the average thickness decreased with the distance (gap) between the Mo fingers. Fig. 1c shows a comparison between the high-resolution SEM images acquired from the 2D-MoS_2 layer grown between the source-drain Mo fingers at a distance of 15 μm and 20 μm, for samples #15 μm and #20 μm, respectively. As can be seen, isolated MoS_2 flakes more frequently appear in the #20 μm sample than #15 μm. Moreover, distinct conductive channels of interconnected flakes between the Mo electrodes were formed in the #20 μm sample, some of which were interrupted. The fluctuation in flake density is also associated with the fluctuation in average thickness found by local μ-Raman measurements for different positions of the laser spot. Representative Raman spectra in the frequency range of the specific A_{1g} and E^1_{2g} peaks for MoS_2 acquired from the devices with different size gaps between the Mo fingers are shown in Fig. 1d. The frequency difference Δ between these peaks could be used to evaluate the mean thickness of a varying number of MLs based on the calibration given in ref. 67. As revealed by the inset in Fig. 1d, the mean thickness decreased with an increase in the gap between the electrodes from 5 μm to 15 μm, with the Δ value decreasing

from 25.5 cm^{-1} (~6 MLs) to 23.0 cm^{-1} (~3 MLs). A fluctuation in the thickness in the range of 2.7–3.6 and 2.4–6.0 MLs was clearly detected in #15 μm and #20 μm, respectively, as shown by the results from the data of Fig. 1d inset. These large thickness fluctuations indicate that the thin intercalated flakes of 1–2 ML thickness have a large probability to be components of channels, thus controlling their conductance. Additionally, the larger number of interconnected flakes, with the corresponding grain boundaries and edge defects in the #15 μm and #20 μm devices make them promising for sensing adsorbed molecules.

3.1 Molecule adsorption effects on gate voltage dependence

The gate voltage dependence of I_{sd} (V_{sd} = 1.0 V) in the #15 μm and #20 μm samples in the dark and under illumination with monochromatic light, under vacuum of different pressures and in the air (at atmospheric pressure) is presented in Fig. 2, showing similar behavior. Specifically, an increase dark current and current during light exposure under vacuum in comparison with the I_{sd} currents measured in air. For better comparison between samples, the current in Fig. 2a and b was normalized to the total area of the 2D-MoS_2 active layer between finger contacts measured in squares of L^2 area (L is the channel length of 15 μm and 20 μm and samples #15 μm and #20 μm have 48□ and 28□ squares, respectively). The normalized I_{sd} (pA/□) represents the product $\sigma_{sd}V_{sd}$ of the surface conductivity, σ_{sd}, and source-drain voltage, V_{sd}.

At V_g = 0 V, in the dark, sample #15 μm was depleted at atmospheric pressure and weakly n-doped under vacuum (Fig. 2a). Removal of the adsorbed molecules from the surface made electrons available for electronic transport and the current reached about 1.0 pA/□. Sample #20 μm was depleted in the dark at all pressures at V_g = 0 V and much larger positive voltages were needed to accumulate free electrons (Fig. 2b). Specifically, a 4.4-times lower current density at the same voltage (2.0 V) above the turn-on voltage flowed through the #20 μm device than the #15 μm (*e.g.* 1.75 pA/□ at V_g = 2 V for #15 μm device and 0.40 pA/□ at V_g = 5 V for #20 μm device, both in the dark and in air). This means that the #20 μm device had more electron traps. As shown in Fig. 1c, the lower density of interconnected MoS_2 flakes, forming separated conductive channels, some of which were interrupted in #20 μm, may also explain its lower surface conductance.

Illumination introduces a larger density of free electrons, as can be seen from the shift in the turn-on voltage of both devices. The #15 μm sample was already turned on at −2 V, while the #20 μm sample turned-on at around −2 V. The shift in the turn-on voltage was larger for the latter device, which indicates that the

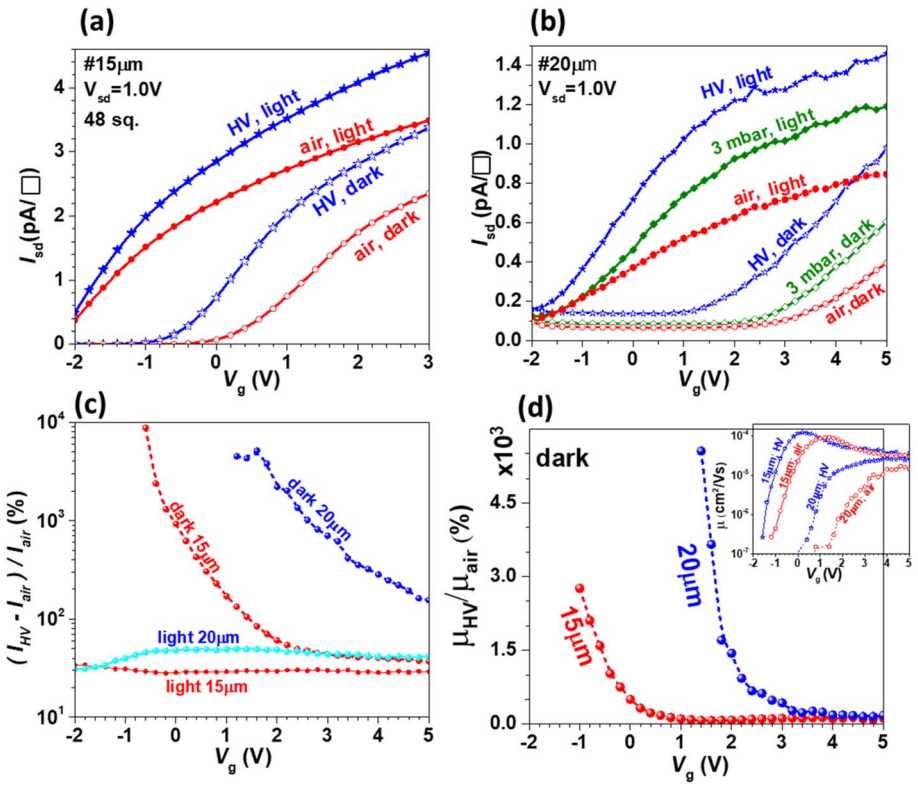

Fig. 2 Gate-voltage dependence of dark source-drain current and photocurrent under monochromatic light measured on samples at room temperature: (a) #15 μm (light of λ = 600 nm) and (b) #20 μm (light of λ = 570 nm) samples under vacuum, in air at atmospheric and reduced pressures (current normalized to the number of L^2 squares (sq.) of the active MoS_2 area, where L is the respective channel length); (c) relative differences between currents measured at high vacuum (HV) of 2 × 10^{-5} mbar (I_{HV}) and in air (I_{air}) at atmospheric pressure on samples #15 μm and #20 μm (relative differences $(I_{HV} - I_{air})/I_{air}$ for dark current and photocurrent under illumination with monochromatic light are shown); and (d) gate voltage dependence of mobility ratio μ_{HV}/μ_{air} obtained from the dark transfer curves in (a) and (b) measured in air and at HV (the absolute values are shown in the inset).

photogenerated carriers reduced the potential disorder, freeing more trapped electrons than in the #15 μm sample. Despite the screening of the disorder by extra electrons, the #20 μm sample remained more sensitive to air molecules on its surface. This is better revealed by the changes in the source-drain currents due to molecular desorption at HV of 2×10^{-5} mbar relative to the values measured in air, as depicted by the gate voltage dependence of $(I_{HV} - I_{air})/I_{air}$ in Fig. 2c for both samples #15 μm and #20 μm. The relative response of the illuminated samples to a change in pressure was weak, and also very weakly dependent on the gate voltage in both samples, but weaker in sample #15 μm with a 30% change in comparison to the 50% change in the #20 μm sample. In contrast, the relative response of the dark current to vacuum reached values up to 1000% at the turn-on voltage. Upon increasing the carrier concentration with a positive gate voltage, the response tended to the value of the illuminated sample, indicating that electrostatic screening of the molecules on the surface is the reason for the lower relative sensitivity under light.

The FET mobility, μ, can be evaluated by dividing the derivative of the normalized dark current I_{sd} (pA/□) in Fig. 2a and b to the product of the voltage $V_{sd} = 1$ V and capacitance $C_i = 1.15 \times 10^{-4}$ F m^{-2} of the 300 nm SiO_2 layer: $\mu = (dI_{sd}(A/□)/dV_g)/(V_{sd}C_i)$. The increase in vacuum mobility μ_{HV} relative to that in air μ_{air} is shown in Fig. 2d by the gate voltage dependence of the μ_{HV}/μ_{air} ratio. It can be seen that there is a huge increase in the vacuum mobility, of orders of magnitude at voltages close to the turn-on voltage, for both the #15 μm and #20 μm samples, similar to the relative change in the dark current ratio $(I_{HV} - I_{air})/I_{air}$ in Fig. 2c. The gate voltage dependence of the FET mobility used to calculate the μ_{HV}/μ_{air} ratio is illustrated in the inset in Fig. 2d for samples #15 μm and #20 μm in the dark and in air or HV. The curves shifted towards positive gate voltages when going from vacuum to air, similarly to the dark current curves in Fig. 2a and b, which can be interpreted as an equivalent p-type doping induced by the adsorption of molecules from air.

The mobility increased be an order of magnitude above the turn-on voltage, but the maximum value remained in the order of 10^{-4} cm^2 V^{-1} s^{-1}. Similarly, a very low FET mobility of $\sim 10^{-4}$ cm^2 V^{-1} s^{-1} has also been reported for MoS_2 obtained by sulfurization of pre-deposited evaporated MoO_2 films.[53] The quality of 2D-MoS_2 films obtained by the sulfurization of pre-deposited MoO_x thin films was also investigated in ref. 58 and 59 by Raman analysis, showing that the residual MoO_3 content in the films decreased with an increase in the growth temperature from 700 °C to 800 °C, resulting in a change from strong p-type doping ($\sim 10^{13}$ cm^{-2}) for the growth temperature of 700 °C to n-type doping (0.04×10^{13} cm^{-2}) for growth at 800 °C. In our FETs with MoS_2 selectively grown at 750 °C by Mo-CVD, clear intrinsic n-type doping was detected, which is typically reported for CVD vapor transport layers that have a negligible Mo oxide content. Thus, it seems that the Mo-CVD mechanism is closer to that of CVD than to that of local sulfurization of an Mo oxide layer.

As also discussed in Introduction, the high device sensitivity to the molecule adsorption can be explained by the high density of edge and grain boundary defects as preferential adsorption sites,[32–34] but a high defect density strongly affects the field effect characteristics by charge trapping, which results in low current and mobility values, depending on the device fabrication methods and measurement conditions (contacts resistance, free surface passivation and contact resistance). As shown in our previous publication, the surface resistivity R (Ω/□) increased nonlinearly by ~24 times when the channel length increased only 4 times (from 5 to 20 μm), and this result was explained by the variation in the density of interconnected flakes and their thickness.[63] Low conductivity close to that of undoped MoS_2 is preferred for higher sensitivity to external stimuli. Therefore, in this study, we chose to investigate the sensitivity to molecule adsorption on larger channel devices (15 and 20 μm).

The very low mobility of our FETs can be explained by their high density of intrinsic defects, grain boundaries of the interconnected flakes, and surface and interface defects, and also by the particular construction of the device. The low current can be further explained by the fact that the MoS_2 coverage of the FET channel was not 100%, especially for the #20 μm sample, as illustrated in Fig. 1c. In the case of our devices, the simplest FET fabrication method was adopted, *i.e.* the pre-deposited Mo used for the selective growth of MoS_2 was directly bonded for FET electrical measurements just after the growth of MoS_2, without additional metallization photolithographic patterning. In this way, contamination of the MoS_2 surface with the inevitable photoresist residue after the photolithographic process was avoided, which could have influenced the adsorption effect of the molecules studied in this work. In ref. 51, a protective SiO_2 layer that was selectively etched on the contact areas was used to significantly improve the metal contact with MoS_2, and thus the FET mobility. This procedure is useful for improving a top-gate FET, but not a bottom-gate FET, which must have the MoS_2 surface uncovered for molecule adsorption detection. The aging effect of 2D-MoS_2 by prolonged exposure to air should also be considered in evaluating the FET performance. In ref. 52, it was shown that the MoS_2 FET sensors based on single MoS_2 flakes exfoliated from the bulk were more stable after intentional aging for a month, but their electrical mobility was significantly reduced from 1–8 cm^2 V^{-1} s^{-1} to 0.5 cm^2 V^{-1} s^{-1}. In our case, the molecule adsorption experiments were performed after 3 months aging of the MoS_2 samples, and care was taken to obtain reproducible characteristics by repeating the air–vacuum changes and the electric measurement cycles to eliminate intermediary hysteresis states. In ref. 52, it was also shown that by exposure to different solvent vapors, the drain current changed in positive (60−300%) and negative (−75 to −98%) ranges for polar and non-polar molecules, accompanied by modification in low-frequency noise. Interestingly, we also performed some tests exposing our devices to acetone vapor and found an exponential increase in the source-drain current during exposure toward a saturation value (~an order of magnitude), as well as unexpectedly large fluctuations in the dc current, which we interpreted as the effect of trapping–detrapping fluctuations of adsorbed polar molecules.

In conclusion, our devices exhibited good sensitivity to molecule adsorption, but for better FET electronic performance, further optimization of the selective MoS_2 growth and device fabrication processes is required.

3.2 Time dependence of the current for light and molecule adsorption excitations

The time-resolved response of I_{sd} to variations in air pressure and illumination is exemplified in Fig. 3a and b for samples #15 μm and #20 μm, respectively. The experiments shown in Fig. 3 started at atmospheric pressure in the dark after the devices reached a constant source-drain current.

The device response times for different stimuli (voltage, light, and air/vacuum exposure) were between a few seconds and minutes, or even longer in the case of molecule adsorption (Fig. 3). This is mainly an electronic effect of changing the concentration of free carriers by deep-level trapping on the surface- and interface-electronic states, or on structural defects in the "bulk" of the 2D MoS_2 few-layers flakes, and by electron transfer or field-induced doping in the case of molecule adsorption and gate voltage variations. In the case of light stimulus, the phenomenon is known as persistent photoconductivity,[68] which has been shown in some cases of ultraviolet light exposure to have a decay-time constant of ~30 days.[69]

In Fig. 3a, in period 1 (between zero and 115 min), the sample in air was subject to two on–off illumination cycles. From the initial value (when the sample was in the dark), the I_{sd} current increased by two orders of magnitude in response to turning on monochromatic light (600 nm wavelength). The current reached 40–50 pA and was not saturated within ~30 min. The first part of relaxation of the current with time, t, upon turning the light on or off at time t_o can be well represented by the superposition of two exponential decay functions, $A_1 \exp(-(t - t_o)/\tau_1) + A_2 \exp(-(t - t_o)/\tau_2)$, where τ_1 and τ_2 are the relaxation times A_1 and A_2 are coefficients (positive or negative for light on and off, respectively). Almost the same relaxation times, τ_1 (80–85 s) and τ_2 (700–800 s), were found for on and off light excitation. A similar response with a slow decrease in current after illumination was observed during the second illumination cycle. After 40 min in the dark following the second illumination pulse, the dark current did not relax to the initial value at the beginning of the experiment. Pumping the cryostat with the sample to 4 mbar, which started at t = 115 min, did not change the current decay, which continued to drop after the last light exposure.

The reaction of I_{sd} to the turning on the turbo molecular pump (TMP) to achieve a high vacuum (HV) of 2×10^{-5} mbar (Fig. 3a, period 2) in the dark was relatively fast. The I_{sd} dark current increased in sub-period 2a and reached saturation of ~40 pA at HV. This current increase can be assigned to the desorption of molecules, mainly O_2 and H_2O. Under high vacuum, the current further increased to ~76 pA upon illumination (sub-period 2b) and relaxed back to ~40 pA upon switching the light off (sub-period 2c), having almost the same values of relaxation times τ_1 and τ_2 as that at atm pressure, further suggesting that the photo-carrier recombination is a bulk phenomenon in the #15 μm sample, which is less dependent on surface recombination centers induced by the adsorbed molecules.

By switching off the turbo-molecular pump, the pressure increased slowly to 2 mbar, which was maintained by the fore-pump (period 3). During the pressure increase, the dark current, I_{sd}, first increased sharply, and when the pressure reached the value of 2×10^{-2} mbar, it later steadily decreased below the value at the beginning of the period 3. The occurrence of the current peak at 2×10^{-2} mbar was verified by repeating the experiment. The time evolution of I_{sd} during increasing the pressure can be explained by H_2O adsorption, which can to induce electron accumulation due to its multiple preferential adsorption sites and molecule orientations, as discussed above related to the schematic in Fig. 1a and in the Introduction.[31–34] The data can be explained if we assume that initially during the adsorption process, water molecules are electrostatically

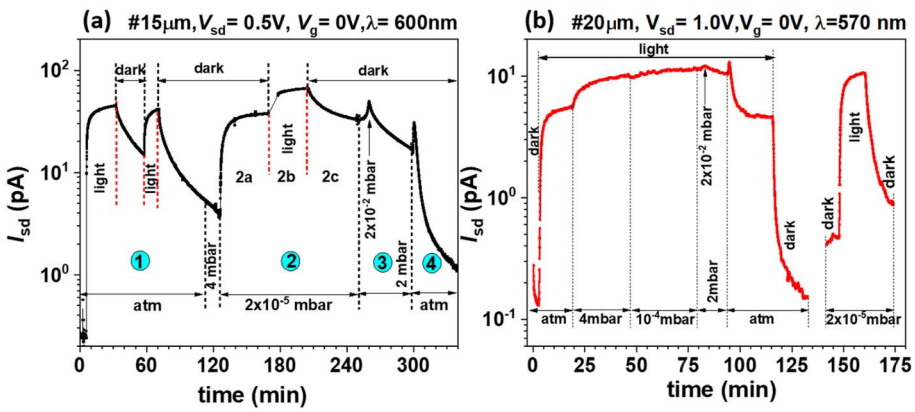

Fig. 3 Time dependence of the source-drain current, I_{sd}, during on–off illumination cycles and vacuum–air pressure variations at room temperature and $V_g = 0$ for samples #15 μm (a) and #20 μm (b). Labels above the figures indicate V_{sd} and V_g voltages during the measurements and light wavelength, λ; air at atmospheric pressure is labeled as "atm". Pressures of 2–4 mbar were obtained by pumping with a fore-vacuum pump, and those below 10^{-4} mbar with turbo-molecular pumps. Different time intervals in panel (a), labeled as 1–4, correspond to constant air pressure times.

adsorbed, with their positive pole towards the MoS_2 surface due to the H^+–S^- attractive interaction, inducing the accumulation of electrons, which generates the current peak at 2×10^{-2} mbar. Over time and by increasing the pressure, the water molecules are adsorbed on the surface of the MoS_2 layer in a more stable position, which is the one with the depletion effect induced by charge transfer (see the schematic in Fig. 1a). The last period, 4, in Fig. 3a corresponds to the rapid introduction of air at atmospheric pressure. The adsorption of molecules starts in period 4 by increasing the dark current, I_{sd}, which forms a current spike similar to that produced by increasing the pressure to 2×10^{-2} mbar in period 3. The current strongly decreased after that due to the electron-depletion effect of the dominant adsorption mode of H_2O and O_2 molecules.

As shown in Fig. 3b, the monitoring of current I_{sd} of sample #20 μm started when monochromatic light (wavelength 570 nm) was turned on with the sample in air at atmospheric pressure. As was the case for the #15 μm sample, the current increased rapidly by over an order of magnitude upon illumination, from the I_{sd} of ∼0.1 pA to 5.5 pA. The huge photo-response with respect to the steady state dark current, as also observed in #15 μm sample (Fig. 3a, two orders of magnitude increase of I_{sd}), can be explained by the combination of photocarrier generation and hole trapping, which increases the electron concentration to keep local charge neutrality. The relaxation times τ_1 and τ_2 are 50 s and 300 s, respectively, which are almost a half of the values for sample #15 μm.

The light exposure of sample #20 μm was constantly maintained during the vacuum experiments in Fig. 3b until $t =$ 115 min. The total I_{sd} current increased at 4 mbar by a factor of 2 ($I_{sd} = 10$ pA). Only a slow, 10%, increase in total current occurred ($I_{sd} = 11.7$ pA) when the vacuum further increased to 10^{-4} mbar. Also, in contrast to the measurement in the dark on sample #15 μm (period 3 in Fig. 3a), under light, there was a weaker decrease in the total current by increasing the pressure back to 2 mbar. The I_{sd} current peak at 2×10^{-2} mbar was observed very clearly in the dark current of sample #15 μm, while for sample #20 μm under illumination it was much weaker, with a temporary increase in current by 10%. The rapid insertion of air at atmospheric pressure at $t = 93$ min in Fig. 3b resulted in a sharp peak of I_{sd}, followed by a decrease towards a lower value ($I_{sd} = 4.6$ pA), close to that measured initially (at $t = 0$) at atmospheric pressure. This is again similar behavior to the dark current in sample #15 μm (period 4 in Fig. 3a). By switching off the light at $t = 115$ min, the dark current in air at atmospheric pressure decreased within ∼15 min close to the value of 0.1 pA, the same as at the beginning of the experiment.

To evaluate the relaxation times of the light excitation response in sample #20 μm under high vacuum, we performed the measurement presented in Fig. 3b starting at $t = 140$ min. The values of response times τ_1 and τ_2 for sample #20 μm measured under high vacuum are 50 s and 280 s for the light on and 35 s and 180 s for light off, respectively. These are shorter than that measured at atmospheric pressure and found for sample #15 μm. This is consistent with the higher density of thinner flakes that dominate the conduction path in larger electrode-gap devices and have faster photocarrier recombination.

3.3 Molecule adsorption effects on spectral photocurrent

The spectral dependence of the photocurrent (defined as the difference between I_{sd} under illumination and I_{sd}^{dark} in the dark before spectral illumination) measured on samples #15 μm and #20 μm under vacuum at different pressures and in air at atmospheric pressure is shown in Fig. 4a and b for gate voltage $V_g = 0$ V. The spectral photocurrent was measured by varying the wavelength from 800 nm to 400 nm in 10 nm steps, 30 s per step, and the current acquired at the step end. As shown in Fig. 3, the total current I_{sd} varied on a scale of tens of min, more than two orders of magnitude relative to the long-term dark current, by switching on and off the light. Thus, we can say that the spectral photocurrent presented here with only 30 s per point refers to the faster device response.

In contrast to #15 μm (Fig. 4a), in the #20 μm sample (Fig. 4b), the spectral photocurrent increased with a decrease in the air pressure from atmospheric (atm) to 2–4 mbar (when the sample was evacuated with a fore-vacuum pump, FVP) and to 2×10^{-5} mbar (evacuated with a high-vacuum pump, HV). For better comparison, the spectral responsivity in air at atm pressure and under HV was computed by normalizing the photocurrent to the spectral illumination power. As can be seen in Fig. 4c, the spectral responsivity of sample #15 μm is almost independent of the molecule adsorption and the atm and HV curves almost overlap, with a small blue-shift in energy for the measurements under vacuum. In sample #20 μm, the photocurrent increased under HV by a factor of 2.1 and is lower than that of the #15 μm on the whole spectrum.

The weak photocurrent sensitivity of sample #15 μm to the ambient pressure can be explained if we assume that the spectral photocurrent is mainly controlled by photo-excitation and recombination in the "bulk" of the 2D-MoS_2 layer, which is less influenced by the molecules adsorbed on the surface. This is supported by the red shift in the photocurrent threshold from ∼1.7 eV in sample #20 μm to ∼1.6 eV ∼ in sample #15 μm. Given that the bandgap decreases with an increase in MoS_2 thickness, the reduced photocurrent threshold in sample #15 μm means that the highest photo-conductance path between the contacts leads to thicker interconnected flakes than in sample #20. The dark current of both samples increased by a factor of 2.4–2.8 under HV, as shown in the inset of the Fig. 4c. It can be seen that sample #15 μm is sensitive to gas molecules, but the large number of photogenerated charge carriers screens the effect of molecules on its surface. The increase in dark current under high vacuum and the spectral response to the change in ambient pressure in the selectively grown 2D-MoS_2 agree with the reported sensitivity of annealed MoS_2 monolayers to H_2O and O_2 adsorption, which was observed as a 100-fold increase in light emission efficiency.[30]

In summary, the selectively grown 2D-MoS_2 films were sensitive to adsorbed gases, and thus can be potentially used as gas sensors. The samples responded to air–vacuum changes in the total current in the full range of λ above their bandgap.

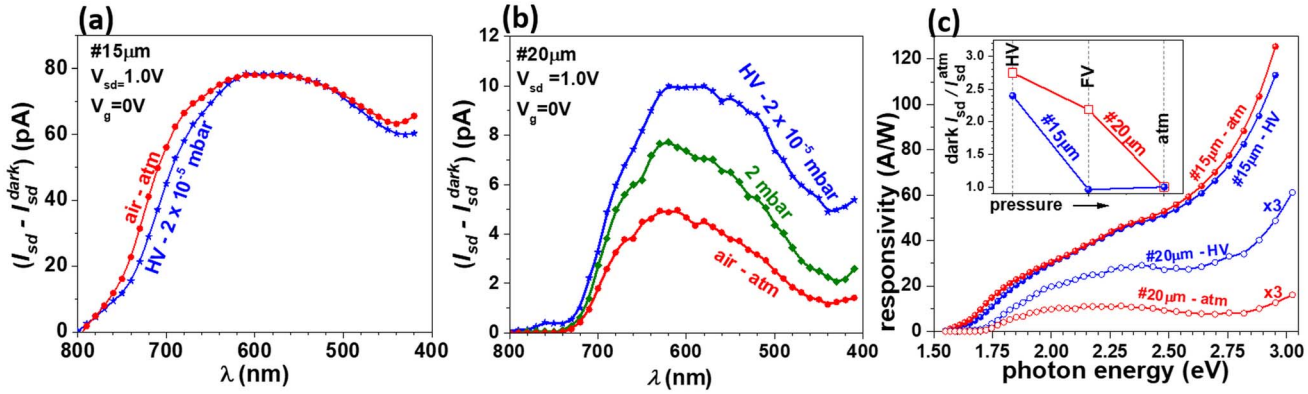

Fig. 4 Spectral photocurrent measured for $V_g = 0$ on samples #15 μm (a) and #20 μm (b) at room temperature under vacuum and at different pressures; and (c) comparison of the spectral photoresponsivity computed based on the data in panels (a) and (b) and the calibrated spectral illumination power (the inset shows the dark current I_{sd} normalized to its value at atmospheric I_{sd}^{atm}).

Similar to the gate dependence, the higher dark conductivity in #15 μm means a lower spectral photocurrent response. The thicker films were conducting at zero gate voltage (Fig. 2a), and thus they can be used as sensors in the two-terminal configuration. In both cases, gate voltage and light can be used to tune the responsivity to molecule adsorption.

3.4 Annealing and temperature dependence of the dark current

We observed that the source-drain dark current flowing through the devices increased when they were placed under high vacuum, which was attributed to the molecule desorption effect. Thus, it was interesting to investigate the high vacuum state of the devices by increasing the temperature to see if the residual adsorbed molecules were further desorbed (supposing that desorption by long-time exposure to high vacuum was not completed). The effect of a stepwise increase in the temperature to 340 K on the samples under high vacuum (2×10^{-5} mbar) is shown in Fig. 5a and b for samples #15 μm and #20 μm, respectively. Each 20 K increase in temperature in Fig. 5a was very fast (21 K min^{-1}) and associated with an initial steep increase in current, followed by a slower decrease at constant temperature plateaus (~60 min annealing). Similar behavior can be seen in Fig. 5b for #20 μm; however, the steep increase in the current is less pronounced and appears as a delayed decrease of the source-drain current. The current measured at 340 K decreased compared with the values measured at 300 K by a factor of 1.8 for #15 μm and of 5.5 for #20 μm. This decrease at a higher temperature was unexpected in the frame of molecule desorption phenomena previously discussed. If we interpret the annealing results in this scenario of molecule adsorption–desorption phenomena, the initial current increase in Fig. 5c suggests the desorption of residual molecules, followed by their readsorption on the energetically more favorable sites. The readsorption should be accompanied by a stronger electron depletion effect to explain the lower current after annealing.

The results obtained by the moderate annealing under high vacuum with a temperature increase of only 40 K can be better explained by the redistribution of the trapped electrons. Thus, the fast temperature increase (21 K min^{-1}) in each step resulted in an initial increase in current due to the electrons thermally activated from the deep traps to the conduction band, as in the well-known thermally stimulated current (TSC) phenomenon.[70] After that, at constant temperature, the exited electrons are trapped in deeper energetic levels, including defects on the surface of MoS_2 and at the interface with the SiO_2 layer, inducing the depletion of free electron concentration in MoS_2 by the field effect. In the literature, by stronger annealing at 200–300 °C, a drastically reduced off-current was reported in thick 2D-MoS_2,[71] but in their case of high temperature annealing in air, the effect was attributed to the internal atomic arrangement of MoS_2 atoms, release of a native point defect at the interface, or even the elimination of photoresist residue included during the fabrication process, similarly to graphene and other 2D-TMD FETs.[64–66]

Following annealing at 340 K under high vacuum, the dark source-drain current in the samples was measured as a function of temperature without breaking the vacuum (4×10^{-6} mbar). The dark I_{sd} measured for both samples by cooling from 340 K to 100 K, and then heating back to 340 K are shown Fig. 5c and d, respectively. These figures also include the curves T_{up} ann. representing the annealing data in Fig. 5a and b, respectively.

The temperature dependence of the current revealed that the conducting film in sample #15 μm showed extrinsic semiconducting-like behavior. When the sample was cooled at the rate of 2.8 K min^{-1}, the current decreased at variable rates (curve T_{down} in Fig. 5c), corresponding to different activation energies, which suggests that the sample contains defects with different trapping energies. Thus, in the range of 340–280 K, the activation energy was 230 meV. The current remained almost constant at the plateau down to 260 K, decreased again with an activation energy of 85 meV, and then 120 meV through a quasi-equilibrium process. This behavior means that the deeper donor state at 230 meV is occupied first during the cool-down, and then the shallow levels at 120 meV below the conduction band. The donor states located 250 meV below the conduction band limit attributed to vacant sulfur vacancies were considered in the model proposed in ref. 45. Using electron paramagnetic

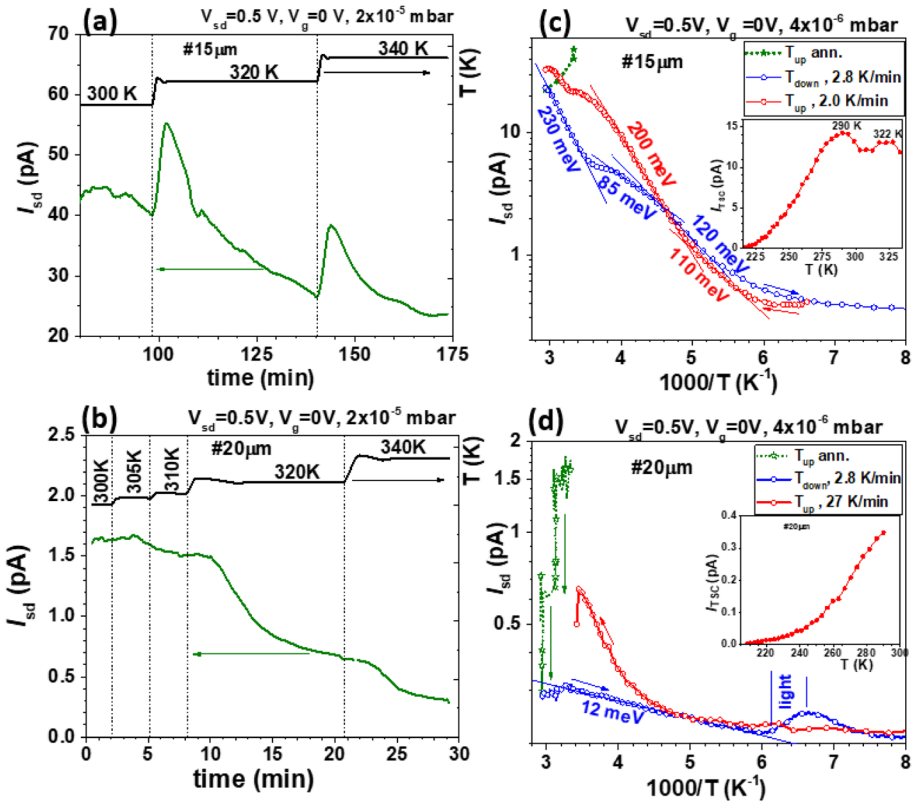

Fig. 5 Temperature dependence of I_{sd} under high vacuum for samples #15 μm (a and c) and #20 μm (b and d): (a) and (b) I_{sd} time dependence during annealing at higher temperatures than RT (T_{up} ann.) and (c) and (d) Arrhenius plot of the I_{sd} temperature dependence for cooling (T_{down}) and heating (T_{up}) at low temperatures. The saturation I_{sd} values at different annealing temperatures (T_{up} ann.) in panels (a) and (b) are also plotted. The insets of (c) and (d) show the corresponding temperature dependence of thermally stimulated current (I_{TSC}).

resonance (EPR), sulfur vacancies and rhenium impurities were identified as defects in natural MoS_2 crystals, in agreement with Hall measurements revealing n-type conductivity with a carrier concentration of 2.3×10^{16} cm^{-3} and mobility of 60 cm^2 V^{-1} s^{-1} at 300 K.[72] Simulating the temperature dependence, they found two activation energies of 89 meV, corresponding to shallow donor states with a concentration of 7×10^{15} cm^{-3} attributed to rhenium impurities; and 241 meV of deeper donor states with a high concentration of 2×10^{19} cm^{-3} related to sulfur vacancies. Based on these literature data, we can attribute the activation energies found in our samples, such as 230 meV, to sulfur vacancies, while 85–120 meV possibly to natural impurities, grain boundaries or disorder defects.

At very low temperatures, the current was almost constant at 0.36 pA, where surface or tunneling-like hopping conduction may dominate the electronic transport. In comparison to cooldown (T_{down} in Fig. 5c), the measurement upon warmup at the rate of 2 K min^{-1} (T_{up} curve in Fig. 5c) shows almost the same constant current of 0.36 pA for $T < 160$ K, followed by an increase with an activation energy of 110 meV (instead of 120 meV for T_{down}-curve) in the interval of 160–210 K. At higher temperatures of 210–300 K, the current increased with an activation energy of ~200 meV and was higher in the T_{up}-curve compared with the T_{down}-curve. This hysteresis of the T_{down}–T_{up} cycle is due to the TSC phenomenon through which, by cooling, free carriers are trapped in the deep levels, and then thermally activated when the temperature increases, generating an additional thermally activated current I_{TSC}.[70] This hysteresis is reduced for a low trap density and low heating rate. This means that the I_{TSC} current (defined as the difference between T_{up} and T_{down} curves, as exemplified by the inset in Fig. 5c) is larger when the temperature increases faster and shows a peak (or more) at a specific temperature (290 °C in this case) depending on the trapping energy level and heating rate. The thermally activated current in our case decreased in the range of 270–300 K when the current activation energy became closer to that of the T_{down} curve.

Transport through the #20 μm sample upon cooldown (curve T_{down} in Fig. 5d) was almost independent of the temperature (activation energy of 12 meV) and the current was very low, suggesting that there is a very low concentration of free carriers in the film and the dominant current flows *via* tunneling, *e.g.* hopping between different states on the surface or in the bulk. The small increase in the current during illumination at 150–160 K verifies that the current flows through the film and induced the filling of deep traps with nonequilibrium electrons. During the fast warmup (at a rate of 27 K min^{-1}), electrons are thermally activated from the traps and generate an I_{TSC} above 210 K (see inset of Fig. 5d).

The investigations presented herein show the complexity of the response of the field-effect device based on interconnected

selectively grown 2D-MoS_2 flakes, a multifunctional device very sensitive to changes in various external stimuli (V_g and V_{sd} voltages, light, molecule adsorption, carrier trapping and temperature). The large number of defects in the film volume and at the surface/interface and grain boundaries had a strong influence on the measurements. The data in Fig. 2–5 demonstrate the strong and complex dependence of the source-drain current in the devices on the pressure of air and the associated molecules adsorbed on the sample surface. This is consistent with the transport and photoluminescence data of the samples prepared by exfoliation or CVD.[30,40] Typically, two types of air molecules were considered in these reports, O_2 and H_2O. Their effect is most often studied, both theoretically and experimentally, for perfect monolayers. In a monolayer, adsorbed O_2 is theoretically predicted to introduce a deep acceptor level in the bandgap.[33] This means that O_2 can trap electrons from the conduction band and its desorption under vacuum would lead to a higher electron density and conductance. This is consistent with the significantly lower dark current and photocurrent in air than under high vacuum but it does not explain the reduction in current upon annealing under vacuum or the current spikes in Fig. 4a and 5a. Although water molecules have been predicted to cause a small increase in the valence band energy at the K-point in monolayer MoS_2, a very large influence of adsorbed H_2O molecules on carrier recombination and photoluminescence in the monolayer was demonstrated.[30] In addition, the devices presented in this study contain regions of thicker layers, which have different band structures. Therefore, the interactions of polar molecules of water with charge carriers in the presented devices with thicker layers must be also considered. It is possible that when water is first adsorbed, it increases the current (carrier concentration) *via* its electric dipole orientation (Fig. 4a) to then reorient itself to be neutral (when aligned parallel to the surface) or even reversing the dipole moment, lowering the current in a steady state.

4. Conclusions

In conclusion, we investigated the sensitivity of field-effect structures based on 2D-MoS_2 layers selectively grown *via* the Mo-CVD method to molecule adsorption. These devices, which were fabricated using the bottom-up approach, consisted of layers of 2D-MoS_2 interconnected flakes selectively grown between pre-deposited Mo source and drain electrodes spaced by 15 μm or 20 μm. The effects of the air pressure, light exposure and gate voltage on the current voltage were measured. It was found that both types of samples (#15 μm and #20 μm) responded similarly to changes in molecular adsorption (mainly H_2O or maybe O_2 from the air) by vacuum-level variations. In both samples, the dark current decreased at atmospheric pressure due to molecule adsorption, which caused electron depletion in MoS_2. Multiple possible adsorption sites and molecule orientations for H_2O relative to the MoS_2 surface producing the depletion or accumulation of electrons can explain the evolution of the current with the air pressure. The response to the light on–off excitation was very high (orders of magnitude), but very slow, resulting from the cumulative effect of photocarrier generation and hole trapping, which increased the electron concentration by maintaining local charge neutrality. In the case of on and off light excitation of the #15 μm sample, almost the same relaxation times, τ_1 (80–85 s) and τ_2 (700–800 s), were found for HV and atmospheric pressure. A faster response to light excitation was found in the #20 μm sample with smaller values of τ_1 (35–50 s) and τ_2 (180–300 s). The dark current was investigated as a function of temperature after annealing the samples up to 340 K under HV. The two samples differed significantly in current values and activation energies. The differences between the #15 μm and #20 μm samples can be explained by the higher density of thinner flakes in the latter sample, which limited the current. The presented results demonstrate the high sensitivity of the 2D-MoS_2 field-effect structures selectively grown by Mo-CVD to molecule adsorption, as well as the possibility to tune their sensitivity by adjusting the growth on patterned substrates with varying gaps between electrodes. In both investigated samples, the relative response at RT of the dark current to vacuum reached values up to 1000% at the turn-on voltage. The temperature dependence of I_{sd} under high vacuum revealed an activation energy of 230 meV, which can be assigned to sulfur vacancies and other shallow levels (85–120 meV), possibly due to natural impurities, grain edges or disorder defects. This result is significant considering the simple, inexpensive, bottom-up technique for the fabrication of devices that contain non-toxic materials. The demonstration of a large number of structural and boundary defects in selectively grown 2D-MoS_2 interconnected flakes controlling the behavior of the studied FET structures can be of great interest for the future applications of this versatile device fabrication technique in optoelectronics or modern synaptic electronics.

Data availability

Data will be made available upon request.

Author contributions

The manuscript was written with contributions from all authors. All authors have approved the final version of the manuscript.

Conflicts of interest

There are no conflicts to declare.

Acknowledgements

This work was financially supported by a grant from the Ministry of Research, Innovation and Digitization, CNCS-UEFISCDI, project number PN.111-P2-2.1-PED-2021-2457, as well as by the NIMP Core Program Project PC2-PN23080202.

References

1 V. Shanmugam, R. A. Mensah, K. Babu, S. Gawusu, A. Chanda, Y. Tu, S. N. Khorasani, M. Försth, G. Sas and O. Das, *Part. Part. Syst. Charact.*, 2022, **39**, 2200031.
2 H. S. Nalwa, *RSC Adv.*, 2020, **10**, 30529–30602.
3 Md. M. Uddin, M. H. Kabir, Md. A. Ali, Md. M. Hossain, M. U. Khandaker, S. Mandal, A. Arifutzzaman and D. Jana, *RSC Adv.*, 2023, **13**, 33336–33375.
4 D. Gupta, V. Chauhan and R. Kumar, *Inorg. Chem. Commun.*, 2020, **121**, 108200.
5 S. Borghardt, J.-S. Tu, F. Winkler, J. Schubert, W. Zander, K. Leosson and B. E. Kardynał, *Phys. Rev. Mater.*, 2017, **1**, 054001.
6 R. Suzuki, M. Sakano, Y. J. Zhang, R. Akashi, D. Morikawa, A. Harasawa, K. Yaji, K. Kuroda, K. Miyamoto, T. Okuda, K. Ishizaka, R. Arita and Y. Iwasa, *Nat. Nanotechnol.*, 2014, **9**, 611–617.
7 T. Heine, *Acc. Chem. Res.*, 2015, **48**, 65–72.
8 B. Zhu, H. Zeng, J. Dai, Z. Gong and X. Cui, *Proc. Natl. Acad. Sci. U. S. A.*, 2014, **111**, 11606–11611.
9 H. Zeng, J. Dai, W. Yao, D. Xiao and X. Cui, *Nat. Nanotechnol.*, 2012, **7**, 490–493.
10 D. Mouloua, A. Kotbi, G. Deokar, K. Kaja, M. El Marssi, M. Ali and M. Jouiad, *Materials*, 2021, **14**, 3283.
11 N. Thomas, S. Mathew, K. M. Nair, K. O'Dowd, P. Forouzandeh, A. Goswami, G. McGranaghan and S. C. Pillai, *Mater. Today Sustainability*, 2021, **13**, 100073.
12 H. Wang, C. Li, P. Fang, Z. Zhang and J. Z. Zhang, *Chem. Soc. Rev.*, 2018, **47**, 6101–6127.
13 K. Kalantar-zadeh and J. Z. Ou, *ACS Sens.*, 2015, **1**, 5–16.
14 R. Malik, V. K. Tomer, Y. K. Mishra and L. Lin, *Appl. Phys. Rev.*, 2020, **7**, 021301.
15 Y. Li, Q. Li, Z. Wang, Z. Huang, J. Zhu, A. I. Channa, F. Cui, H. Xu, X. Li, L. Zhou and G. Zou, *Appl. Phys. Lett.*, 2023, **123**, 151103.
16 L. M. Xie, *Nanoscale*, 2015, **7**, 18392–18401.
17 G. Swain, S. Sultana and K. Parida, *Nanoscale*, 2021, **13**, 9908–9944.
18 D. Andrzejewski, M. Marx, A. Grundmann, O. Pfingsten, H. Kalisch, A. Vescan, M. Heuken, T. Kümmell and G. Bacher, *Nanotechnology*, 2018, **29**, 295704.
19 L. Yu, M. Deng, J. L. Zhang, S. Borghardt, B. Kardynal, J. Vučković and T. F. Heinz, *Nano Lett.*, 2021, **21**, 2376–2381.
20 D. S. Schneider, A. Grundmann, A. Bablich, V. Passi, S. Kataria, H. Kalisch, M. Heuken, A. Vescan, D. Neumaier and M. C. Lemme, *ACS Photonics*, 2020, **7**, 1388–1395.
21 E. Reato, P. Palacios, B. Uzlu, M. Saeed, A. Grundmann, Z. Wang, D. S. Schneider, Z. Wang, M. Heuken, H. Kalisch, A. Vescan, A. Radenovic, A. Kis, D. Neumaier, R. Negra and M. C. Lemme, *Adv. Mater.*, 2022, **34**, 2108469.
22 J. Wu, J. Liu, J. Cui, S. Yao, M. Ihsan-Ul-Haq, N. Mubarak, E. Quattrocchi, F. Ciucci and J.-K. Kim, *J. Mater. Chem. A*, 2020, **8**, 2114–2122.
23 T. Stephenson, Z. Li, B. Olsen and D. Mitlin, *Energy Environ. Sci.*, 2014, **7**, 209–231.
24 N. Joseph, P. M. Shafi and A. C. Bose, *Energy Fuels*, 2020, **34**, 6558–6597.
25 Y. Zhang, Y. Gao, S. Yao, S. Li, H. Asakura, K. Teramura, H. Wang and D. Ma, *ACS Catal.*, 2019, **9**, 7967–7975.
26 G. Giuffredi, T. Asset, Y. Liu, P. Atanassov and F. Di Fonzo, *ACS Mater. Au*, 2021, **1**, 6–36.
27 X. Wang, L. Meng, B. Li and Y. Gong, *Mater. Today*, 2021, **47**, 108–130.
28 P. Luo, F. Zhuge, Q. Zhang, Y. Chen, L. Lv, Y. Huang, H. Li and T. Zhai, *Nanoscale Horiz.*, 2019, **4**, 26–51.
29 X. Zhang, Z. Shao, X. Zhang, Y. He and J. Jie, *Adv. Mater.*, 2016, **28**, 10409–10442.
30 S. Tongay, J. Zhou, C. Ataca, J. Liu, J. S. Kang, T. S. Matthews, L. You, J. Li, J. C. Grossman and J. Wu, *Nano Lett.*, 2013, **13**, 2831–2836.
31 Y. Wang, S. M. Gali, A. Slassi, D. Beljonne and P. Samorì, *Adv. Funct. Mater.*, 2020, **30**, 2002846.
32 R. Wang, X. Wang, Z. Zuo, S. Ni, J. Dai and D. Wang, *Molecules*, 2022, **27**, 8710.
33 F. Ferreira, A. Carvalho, Í. J. M. Moura, J. Coutinho and R. M. Ribeiro, *J. Phys.: Condens. Matter*, 2017, **30**, 035003.
34 N. S. Bobbitt, J. F. Curry, T. F. Babuska and M. Chandross, *RSC Adv.*, 2024, **14**, 4717–4729.
35 E. Akbari, K. Jahanbin, A. Afroozeh, P. Yupapin and Z. Buntat, *Phys. B*, 2018, **545**, 510–518.
36 D.-W. Lee, J. Lee, I. Y. Sohn, B.-Y. Kim, Y. M. Son, H. Bark, J. Jung, M. Choi, T. H. Kim, C. Lee and N.-E. Lee, *Nano Res.*, 2015, **8**, 2340–2350.
37 H. Li, Z. Yin, Q. He, H. Li, X. Huang, G. Lu, D. W. H. Fam, A. I. Y. Tok, Q. Zhang and H. Zhang, *Small*, 2011, **8**, 63–67.
38 F. K. Perkins, A. L. Friedman, E. Cobas, P. M. Campbell, G. G. Jernigan and B. T. Jonker, *Nano Lett.*, 2013, **13**, 668–673.
39 A. L. Friedman, F. K. Perkins, E. Cobas, G. G. Jernigan, P. M. Campbell, A. T. Hanbicki and B. T. Jonker, *Solid-State Electron.*, 2014, **101**, 2–7.
40 A. Di Bartolomeo, A. Kumar, O. Durante, A. Sessa, E. Faella, L. Viscardi, K. Intonti, F. Giubileo, N. Martucciello, P. Romano, S. Sleziona and M. Schleberger, *Mater. Today Nano*, 2023, **24**, 100382.
41 O. Samy, S. Zeng, M. D. Birowosuto and A. El Moutaouakil, *Crystals*, 2021, **11**, 355.
42 B. Radisavljevic, A. Radenovic, J. Brivio, V. Giacometti and A. Kis, *Nat. Nanotechnol.*, 2011, **6**, 147–150.
43 Z. Cheng, S. He, X. Han, X. Zhang, L. Chen, S. Duan, S. Zhang and M. Xia, *J. Mater. Chem. C*, 2024, **12**, 2794–2802.
44 A. Di Bartolomeo, L. Genovese, A. C. Ferrari, L. Iemmo, G. Luongo, T. Foller and M. Schleberger, *2D Mater.*, 2017, **5**, 015014.
45 A. Mamun, Y. Sainoo, T. Takaoka, A. Ando and T. Komeda, *RSC Adv.*, 2024, **14**, 36517–36526.
46 Y. Guo, X. Wei, J. Shu, B. Liu, J. Yin, C. Guan, Y. Han, S. Gao and Q. Chen, *Appl. Phys. Lett.*, 2015, **106**, 103109.
47 J. Kim, B. Seo, S. Lee, S. Jeong and Y. Roh, *ECS Trans.*, 2017, **77**, 35–39.

48 S. Ethan Panasci, E. Schilirò, G. Greco, M. Cannas, F. M. Gelardi, S. Agnello, F. Roccaforte and F. Giannazzo, *ACS Appl. Mater. Interfaces*, 2021, **13**, 31248–31259.
49 J. Neilson, M. P. Avery and B. Derby, *ACS Appl. Mater. Interfaces*, 2020, **12**, 25125–25134.
50 J. Jiang, Y. Zhang, A. Wang, J. Duan, H. Ji, J. Pang, Y. Sang, X. Feng, H. Liu and L. Han, *ACS Appl. Electron. Mater.*, 2020, **2**, 2132–2140.
51 P.-Z. Shao, H.-M. Zhao, H.-W. Cao, X.-F. Wang, Y. Pang, Y.-X. Li, N.-Q. Deng, J. Zhang, G.-Y. Zhang, Y. Yang, S. Zhang and T.-L. Ren, *Appl. Phys. Lett.*, 2016, **108**, 203105.
52 R. Samnakay, C. Jiang, S. L. Rumyantsev, M. S. Shur and A. A. Balandin, *Appl. Phys. Lett.*, 2015, **106**, 023115.
53 H. Kim, T. Park, M. Leem, H. Lee, W. Ahn, E. Lee and H. Kim, *Appl. Surf. Sci.*, 2021, **535**, 147684.
54 Y. Lee, J. Lee, H. Bark, I.-K. Oh, G. H. Ryu, Z. Lee, H. Kim, J. H. Cho, J.-H. Ahn and C. Lee, *Nanoscale*, 2013, **6**, 2821.
55 K. S. Kim, D. Lee, C. S. Chang, S. Seo, Y. Hu, S. Cha, H. Kim, J. Shin, J.-H. Lee, S. Lee, J. S. Kim, K. H. Kim, J. M. Suh, Y. Meng, B.-I. Park, J.-H. Lee, H.-S. Park, H. S. Kum, M.-H. Jo and G. Y. Yeom, *Nature*, 2023, **614**, 88–94.
56 S. H. Aleithan, T. E. Wickramasinghe, M. Lindquist, S. Khadka and E. Stinaff, *ACS Omega*, 2019, **4**, 9557–9562.
57 M. Chiu, H. Tang, C. Tseng, Y. Han, A. Aljarb, J. Huang, Y. Wan, J. Fu, X. Zhang, W. Chang, D. A. Muller, T. Takenobu, V. Tung and L. Li, *Adv. Mater.*, 2019, **31**, 1900861.
58 S. E. Panasci, E. Schilirò, A. Koos, F. Roccaforte, M. Cannas, S. Agnello, B. Pécz and F. Giannazzo, *Appl. Phys. Lett.*, 2024, **124**, 243101.
59 S. E. Panasci, A. Koos, E. Schilirò, S. D. Franco, G. Greco, P. Fiorenza, F. Roccaforte, S. Agnello, M. Cannas, F. M. Gelardi, A. Sulyok, M. Nemeth, B. Pécz and F. Giannazzo, *Nanomaterials*, 2022, **12**, 182.
60 K.-Y. Yang, H.-T. Nguyen, Y.-M. Tsao, S. B. Artemkina, V. E. Fedorov, C.-W. Huang and H.-C. Wang, *Sci. Rep.*, 2023, **13**, 8378.
61 S. Vangelista, E. Cinquanta, C. Martella, M. Alia, M. Longo, A. Lamperti, R. Mantovan, F. B. Basset, F. Pezzoli and A. Molle, *Nanotechnology*, 2016, **27**, 175703.
62 T. Stoica, M. Stoica, M. Duchamp, A. Tiedemann, S. Mantl, D. Grützmacher, D. Buca and B. E. Kardynał, *Nano Res.*, 2016, **9**, 3504–3514.
63 I. Stavarache, C. Palade, A. Slav, I. Dascalescu, A.-M. Lepadatu, L. Trupina, E. Matei, M. L. Ciurea and T. Stoica, *ACS Appl. Nano Mater.*, 2024, **7**, 5051–5062.
64 Z. Cheng, Q. Zhou, C. Wang, Q. Li, C. Wang and Y. Fang, *Nano Lett.*, 2011, **11**, 767–771.
65 J. P. Merino, S. Brosel-Oliu, G. Rius, X. Illa, M. V. Sulleiro, E. D. Corro, E. Masvidal-Codina, A. B. Calia, J. A. Garrido, R. Villa, A. Guimerà-Brunet, M. Prato, A. Criado and E. Prats-Alfonso, *ACS Sustain. Chem. Eng.*, 2024, **12**, 9133–9143.
66 J. Liang, K. Xu, B. Toncini, B. M. Bersch, B. Jariwala, Y.-C. Lin, J. A. Robinson and S. K. Fullerton-Shirey, *Adv. Mater. Interfaces*, 2019, **6**, 1801321.
67 C. Lee, H. Yan, L. E. Brus, T. F. Heinz, J. Hone and S. Ryu, *ACS Nano*, 2010, **4**, 2695–2700.
68 Y.-C. Wu, C.-H. Liu, S.-Y. Chen, F.-Y. Shih, P.-H. Ho, C.-W. Chen, C.-T. Liang and W.-H. Wang, *Sci. Rep.*, 2015, **5**, 11472.
69 A. George, M. V. Fistul, M. Gruenewald, D. Kaiser, T. Lehnert, R. Mupparapu, C. Neumann, U. Hübner, M. Schaal, N. Masurkar, L. M. R. Arava, I. Staude, U. Kaiser, T. Fritz and A. Turchanin, *npj 2D Mater. Appl.*, 2021, **5**, 15.
70 S. Deb, P. Chakrabarti, H. Chakraborti, K. D. Gupta and S. Dhar, *Appl. Phys. Lett.*, 2019, **115**, 032104.
71 S. D. Namgung, S. Yang, K. Park, A.-J. Cho, H. Kim and J.-Y. Kwon, *Nanoscale Res. Lett.*, 2015, **10**, 62.
72 F. D. Brandão, G. M. Ribeiro, P. H. Vaz, J. C. González and K. Krambrock, *J. Appl. Phys.*, 2016, **119**, 235701.